Materials Research Proceedings 28 (2023) 189-198 https://doi.org/10.21741/9781644902479-21

2D FE modeling of the thermal history of the heat affected zone in AlSi10Mg LPBF

DELAHAYE Jocelyn[1,a], HABRAKEN Anne M.[2,b] and MERTENS Anne[1,c *]

[1]University of Liège, Faculty of Applied Sciences, Aerospace and Mechanics Department, Metallic Materials Science, Quartier Polytech 1, Allée de la Découverte 13A, B-4000 Liège, Belgium

[2]University of Liège, Faculty of Applied Sciences, ArGEnCo Department, Materials and Solid Mechanics, Quartier Polytech 1, Allée de la Découverte 13A, B-4000 Liège, Belgium

[a]jocelyn.delahaye@uliege.be, [b]anne.habraken@uliege.be, [c]anne.mertens@uliege.be

Keywords: Aluminium Alloys, LPBF, Thermal History, Microstructure, Modeling

Abstract. As an easily processable Al alloy, AlSi10Mg manufactured by Laser Powder Bed Fusion (LPBF) has received a lot of attention so far. However, it is well known that microstructural heterogeneities at the scale of the melt pool – in particular the weaker Heat Affected Zone whose microstructure evolves during the deposition of the next layer – exert a strong detrimental effect on the ductility of AlSi10Mg LPBF. In this work, a 2D Finite Element (FE) model is developed in order to tackle this issue and help in guiding the optimisation of LPBF process parameters. The model is calibrated using experimental measurements of the melt pool height. Furthermore, to allow for the efficient simulation of 5 successive layers, a remeshing procedure is implemented. No heat accumulation is observed during the deposition of these 5 layers. The thermal history of the HAZ can thus be studied with a thermal model for one layer.

Introduction

The Laser Powder Bed Fusion (LPBF) of Al alloys has been the subject of extensive work for almost a decade, dating back to the pioneering work of Thijs et al. [1] and Olakanmi et al. [2]. Among the wide variety of available Al alloys, the hypoeutectic AlSi10Mg alloy has received a particular attention in view of its good castability and weldability, its high melt fluidity and low shrinkage upon solidification [3-5]. However, microstructural heterogeneities at the scale of the melt pool remain a matter of concern, by compromising the ductility of AlSi10Mg LPBF components [6,7]. Indeed, the Heat Affected Zone (HAZ) whose microstructure evolves during the deposition of the subsequent layer has been shown to play an essential role in the tensile fracture of AlSi10Mg LPBF. The Si eutectic precipitates that are originally finely distributed in a cellular structure, tend to coarsen and globularize under the influence of the heat input associated to the deposition of next layer, as can be seen in Fig. 1. As a result, the fine cellular structure is broken, thus creating a weaker zone for damage initiation [6]. The microstructural homogeneity and the ductility of AlSi10Mg LPBF components may be restored to some extent by thermal or thermo-mechanical post-treatments but this improvement in ductility is achieved at the cost of a loss in strength [7-9]. As an alternative to post-treatments, optimisation of the processing parameters with the aim of minimizing the thickness of the HAZ appears as a viable option [10]. Physically based and validated Finite Element (FE) models are essential tools in that respect.

In this work, a 2D FE model is developed in order to tackle this issue and help in guiding the optimisation of LPBF process parameters. Two different calibration procedures were tested i.e. using experimental measurements of (1) the cell size or of (2) the melt pool height. Furthermore, to allow for the efficient simulation of 5 successive layers, a remeshing procedure is implemented.

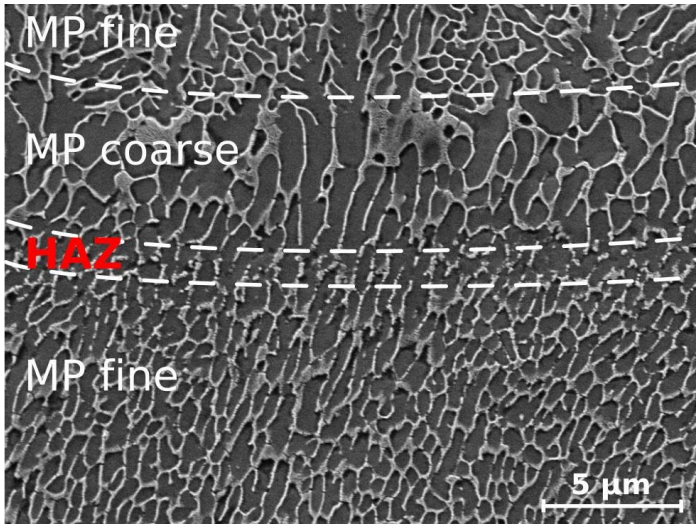

Fig. 1. SEM micrograph showing the fine cellular microstructure at the core of the melt pool (MP fine), the coarser cellular structure at the outskirts of the melt pool (MP coarse) and the Heat Affected Zone (HAZ) where the cellular structure of the fine eutectic Si precipitates is broken and globularized.

Materials and Methods

Sample fabrication.

In order to obtain experimental data for the calibration and validation of the FE model, two sets of AlSi10Mg LPBF samples, named as set A and set B, were fabricated under very distinct processing conditions. Samples of set A were processed using a MTT SLM 250 machine. The building parameters were as follow: a laser power of 175W, a scan speed of 195 mm/s, a powder layer thickness of 60 µm and a pre-heating temperature of 200°C. Samples of set B were fabricated using an EOS SLM equipment and the following processing parameters: a laser power of 370W, a scan speed of 1300 mm/s and a powder layer thickness of 40 µm without pre-heating i.e. considering a building platform temperature of 35°C. Both sets of samples were fabricated in the vertical direction. The processing parameters of set A were chosen to enhance the thickness of the HAZ, as opposed to the processing parameters of set B. More details may be found in [6,8,10].

Characterization.

Samples for microstructural characterization were ground and polished following standard practices and then etched using Keller's reagent (95 vol.% distilled water, 2.5 vol.% HNO_3, 1.5 vol.% HCl and 1 vol.% HF). Scanning electron microscopy was carried out using a Philips XL30 microscope. Image analysis was performed using the ImageJ software to determine the Al Cells size in the MP fine, MP coarse and HAZ (Fig. 1). The melt pool height was only measured on the last deposited layer, since the melt pool of the previous layers are overlapped due to the systematic re-melting of the underlying layer during the deposition of each new layer.

Finite Element model.

A 2D thermal finite element model of the LPBF process has been developed as follows. The temperature evolution in the part is given by the non-linear equation for an isotropic material:

$$\nabla . k\nabla T + Q = \rho c_p \frac{\partial T}{\partial t} \quad (1)$$

where ∇ is the gradient operator; k is the thermal conductivity, Q the power generated in the part, ρ the density, c_p the heat capacity and t the time. The enthalpy of fusion and vaporization are included in the heat capacity that is thus defined as an apparent heat capacity.

The boundary condition at the free surface for the heat exchange is defined as:

$$-k\nabla T.n = q_{laser} - h(T - T_{amb}) - \mathcal{E}\sigma\left(T^4 - {T_{amb}}^4\right) \quad (2)$$

where n is a unit vector normal to the surface; T_{amb}, the ambient temperature, h, the convection coefficient (taken as 20 W/m^{2}K); σ, the Stefan-Boltzmann's constant (5.67×10^{-8} W/m^{2}K^4), $\mathcal{E}$, the emissivity and q_{laser} the laser heat source. The laser is modeled by a Gaussian heat source:

$$q_{laser} = \frac{2AP}{\pi R^2} exp\left(\frac{2r^2}{R^2}\right) \quad (3)$$

where P is the laser power (i.e. 175 W or 370 W); R, the laser beam radius (40 µm); A, the laser absorbed energy; r, the radial distance from the beam centre.

The thermophysical properties are considered temperature dependent. These properties are obtained from [11] for the base plate made from aluminium alloy 2024, and from [8] for the AlSi10Mg powder bed and consolidated part. The laser absorbed energy A is chosen as a tuning parameter of the 2D FE model and is obtained through calibration based on experimental observations. In this study, two different calibration procedures have been tested: (1) based on experimental measurements of the cell size and (2) based on experimental measurements of the melt pool height. The academic finite element code LAGAMINE is used. It is developed since 1984 at the University of Liege [12-15]. To switch between the desactivated elements, the unfused powder, to the bulk material and vary the bulk properties, element birth and death technique is employed. The mesh of the system and boundary conditions are summarized in Fig. 2.

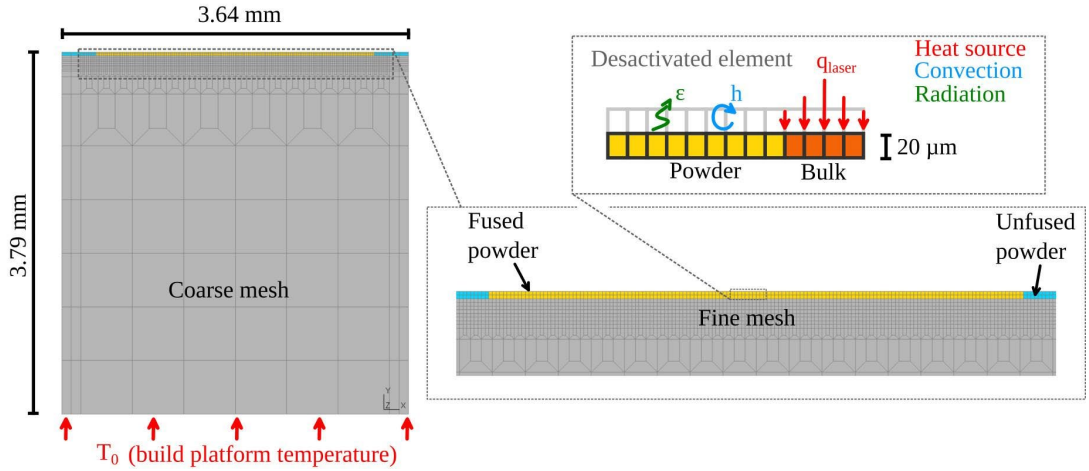

Fig. 2. Finite element domain with the boundary conditions: laser heat source, heat loss by convection, radiation, and build platform temperature. Desactivated elements are illustrated to highlight the birth and death technique.

The dimensions of the studied domain are 3.79 mm in height and 3.64 mm in width, that is large enough for the melt pool to reach a thermal steady state and to reproduce the heat drain effect of the build platform and previous solidified layers. The domain is discretized with 2D quadrilateral elements. Furthermore, the domain is divided in two zones: a fine meshed zone of size ranging from 40 µm to 2.5 µm where the laser is applied, fine enough to capture the steep thermal gradient, and a coarse zone below to save in number of elements and computation time.

In particular, a 2D multilayer simulation of the LPBF process was performed in this work, in order to investigate the effect of the number of fused layers on heat accumulation and thus on the thermal history of LPBF AlSi10Mg components. To reduce the computational costs of this

multilayer model, that can be high even in 2D, a remeshing strategy has been developed in order to keep the number of node constant independently of the number of layers under consideration. It consists in picking the temperature field at the end of the simulation for the first layer and set this temperature as an initial nodal condition for the second layer. This operation is then repeated for the third layer and so forth… As shown in Fig. 3, the change in powder bed height with the number of fused layers is incorporated in the coarse part of the mesh while the fine part remains the same. This approach allows to perform multilayer simulations while keeping the computation time reasonable.

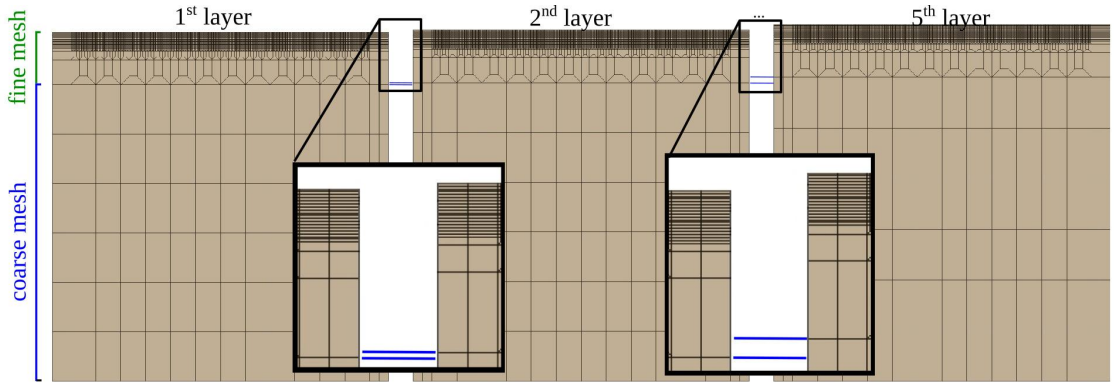

Fig. 3. Meshed domains for the first, second and fifth layer. The number of elements remain constant between the domains. The fine mesh part are the same between the domains while the coarse part changes.

Results and Discussion

Sensitivity to the mesh size.

Convergency was tested based on the size of the fine mesh zone ranging from 40 µm to 5 µm in Fig. 4. Based on the analysis of the line profile in Fig. 4(b) extracted from the temperature maps of Fig. 4(a), mesh convergency is shown. A mesh size of 10 µm offers a good compromise between accuracy and computation time. This is also demonstrated when analyzing the melt pool area with the laser beam travel time in Fig. 4(c). We should notice that it takes 1.8 ms for the melt pool to reach a steady state where its size no longer changes. Therefore, the size of the model is large enough to study the thermal history in the heat affected zone.

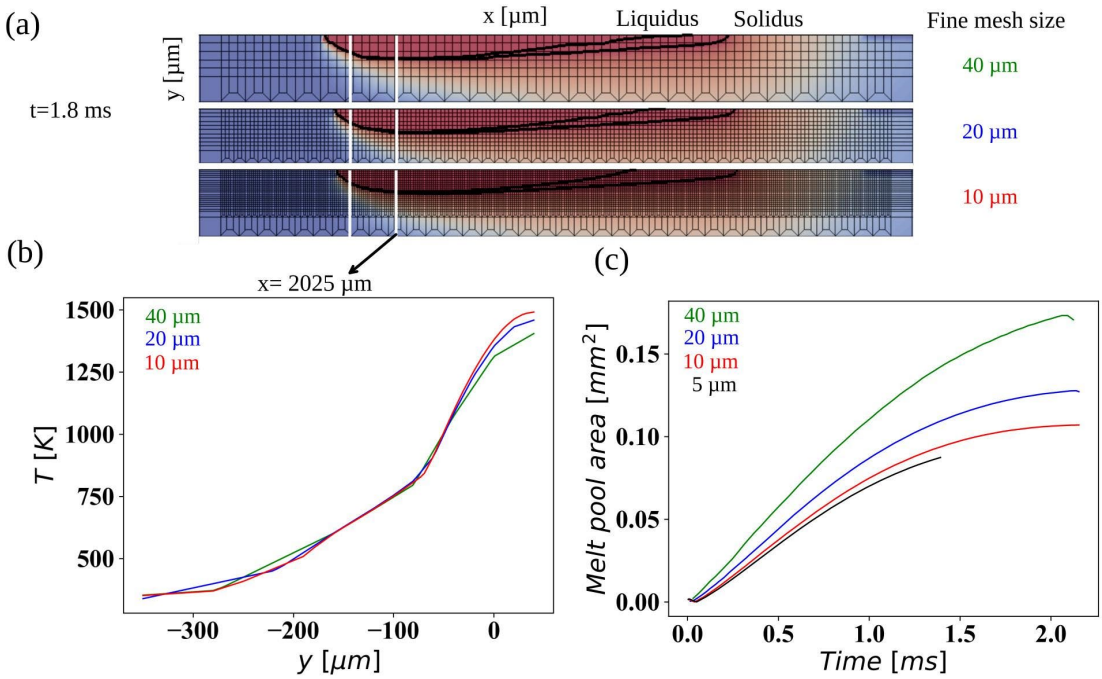

Fig. 4. (a) Temperature map of the melt pool taken at t=1.8 ms for different mesh refinements. (b) Corresponding temperature line profile at x = 2025 µm position and (c) melt pool area with the laser beam travel time.

Model calibration.

The results of the calibration of the 2D thermal model under the processing parameters of set B are shown in Fig. 5(a) for the calibration based on the melt pool height and in Fig. 5(b) for the calibration based on the cell size that can be computed from the cooling rates extracted at the liquidus isotherm line [6,8,10,16]. Fig. 5 shows a remarkable result in that the 2D FE model can only be calibrated against the melt pool height. Indeed, the cell size values computed from the FE model are systematically larger than the experimental values. This is a marked difference to previous reports concerning analytical model as e.g. Rosenthal's model [6,10,16] for which calibration based on cell size may be preferred in view of its greater flexibility as cell size may be measured at any location within the sample contrarily to the melt pool height that is only accessible in the last deposited layer.

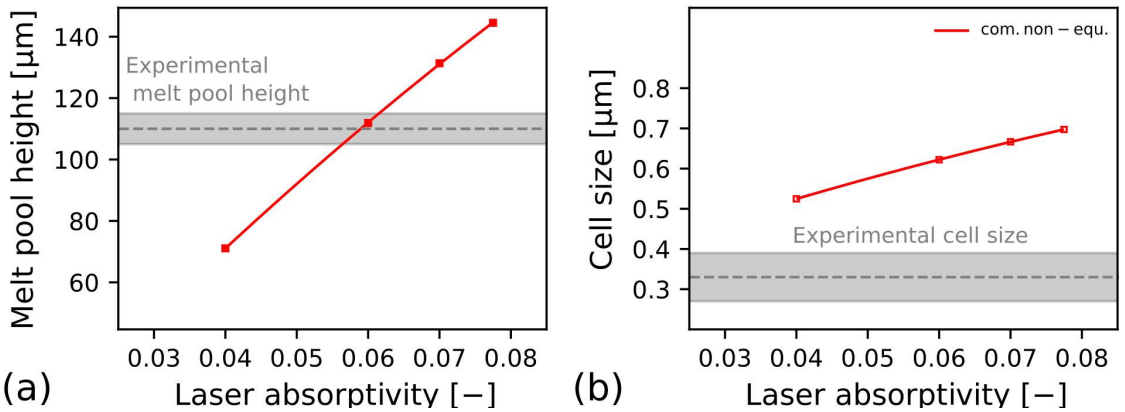

Fig. 5. (a) Melt pool height and (b) cell size calibration for the 2D thermal FE model.

This observation can be understood considering that the cell size is computed from the cooling rate that depends in turn on the thermal gradient. The heat flux transmitted by conduction in the part is also proportional to the thermal gradient. However, in the present 2D FE model, the heat flux is not evacuated through a surface but through a line. In this case, fewer paths are available for these fluxes. Therefore, the 2D model systematically experiences a lower thermal gradient compared to a 3D model. The 2D FE model will thus always overestimate the cell size.

The effect of the number of fused layers for samples of set B is studied by analyzing the thermal history of three points of interest (POIs) in Fig. 6. These POIs are located in such a way that their respective spacings correspond to 2 times the powder bed thickness, i.e. 40 µm. In this way, the thermal history can be compared between the fused layers. As can be seen in Fig. 6, the thermal history of POI1 exhibits five peaks corresponding to the five fused layers. The first peak corresponds to the maximum temperature experienced during the direct application of the heat flux of the laser. In view of the location of the three POIs, the maximum temperature of POI2 is then reached during the fusion of the third layer while the maximum temperature of POI3 is reached for the fifth layer. When comparing the temperature of the first peak for the three POIs, it can be seen that they have the same value around 2700K. In a similar way, the second and the third peaks of POI1 and POI2 match each other with values around 1750K and 1350K, respectively. The good match between the peaks for the three POIs indicates that they is no rise in temperature as the successive layers are fused. Furthermore, this observation is confirmed qualitatively by looking at the temperature distribution around the melt pool in Fig. 6(b-c). Indeed, the temperature distribution and the melt pool size obtained for the first layer (Fig. 6(b)) and for the fifth layer (Fig. 6(c)) are very similar. The cold area at the right-hand side of Fig. 6(c) corresponds to unfused powder.

This observation that the heat accumulation remains negligible during the deposition of five successive layers can be explained by considering both the thermophysical properties of AlSi10Mg and the processing conditions. Indeed, LPBF AlSi10Mg exhibits a high thermal conductivity with values ranging between 110 and 130 $W*m^{-1}*K^{-1}$ [8]. These values are much higher than those reported for LPBF Ti6Al4V (5-34 $W*m^{-1}*K^{-1}$)[17] or stainless steel 316L (14-34 $W*m^{-1}*K^{-1}$) [18] for which heat accumulation is observed. The high thermal conductivity of LPBF AlSi10Mg thus allows the rapid evacuation of heat from the melt pool and its vicinity towards the top surface of the part where it can be dissipated first through radiation just after the laser is switched off and later through convection. Moreover, the high laser scan speed (1300 mm/s) combined with a medium laser power (370W) used for the processing of set B samples result in relatively low heat input when compared to the processing parameters of [17] and [18], which also contributes to the negligible heat accumulation.

Microstructural observation of the HAZ dimensions along the whole sample height brings further confirmation of the above finding. Indeed, the HAZ has been found to exhibit a constant width throughout [8], thus also suggesting that the average temperature in the part remains constant. This result implies that the thermal history of the HAZ in LPBF AlSi10Mg processed under relatively low heat input is independent of the number of fused layers, and that it can be studied using one layer FE thermal model.

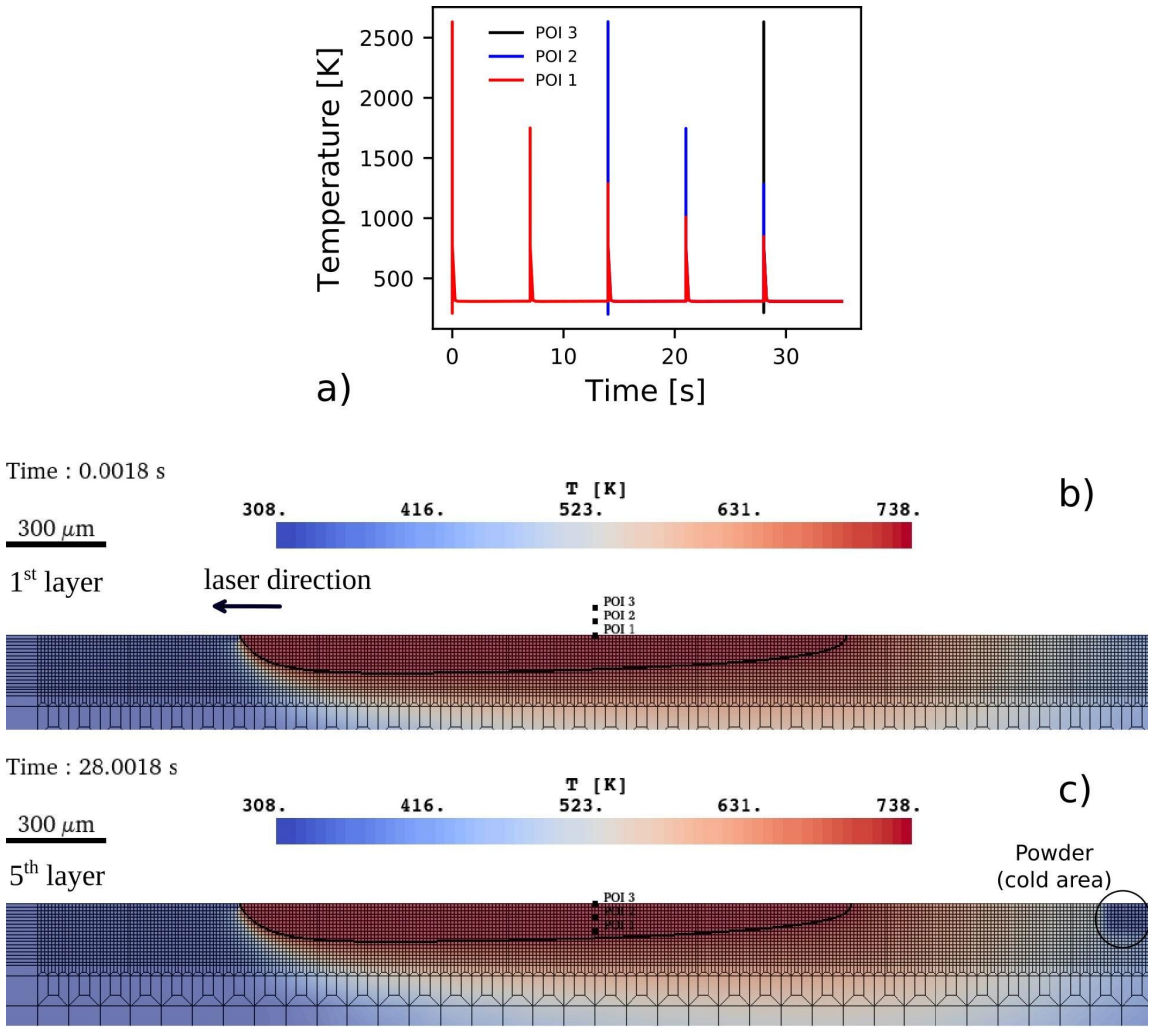

Fig. 6. (a) Thermal history of three POIs; temperature maps (b) for the first layer and (c) for the fifth layer.

The influence of the processing parameters on the thermal history of the HAZ is studied by comparing the result of FE simulations for the two sets of processing parameters A ("Sirris", with a relatively low laser power of 175W, a slow scan speed of 195 mm/s and build platform temperature of 200°C resulting in a relatively high heat input) and B ("Anyshape", with a laser power of 370W, a high laser scan speed of 1300 mm/s and build platform temperature of 35°C resulting in a relatively low heat input). These two parameters sets have been selected as (1) they are far enough from each other to expect different thermal histories and (2) the corresponding microstructures have been characterized in details [8].

The thermal histories in the HAZ for the two sets of processing parameters are plotted in Fig. 7(a). For set B (Anyshape), a peak of temperature is observed at 650K lasting for 1.5 ms. For set A (Sirris), on the contrary, the peak is wider, lasting over 2.5 ms. In the latter case, the end of the peak is not clearly visible as the temperature of the peak does not fall back to 473K, that is the build platform temperature, within the frame of the simulation.

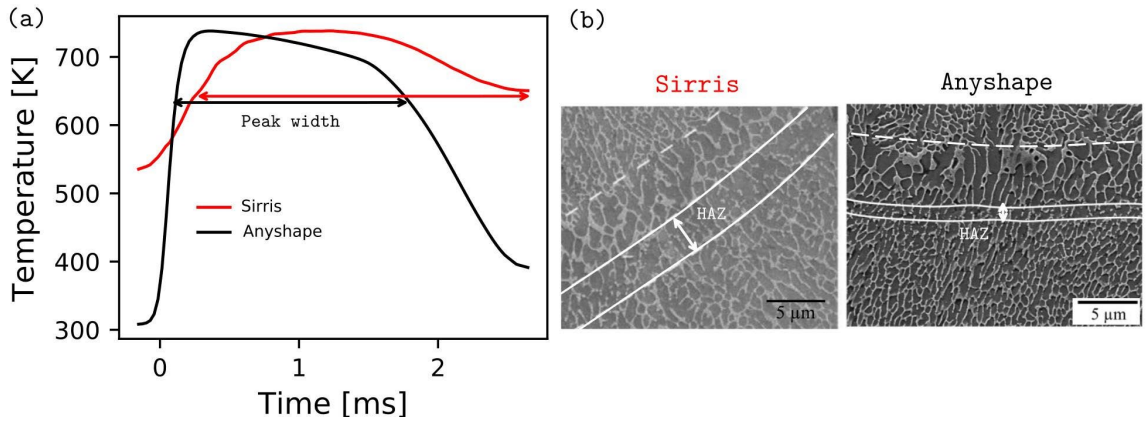

Fig. 7. (a) Thermal history of the HAZ and (b) corresponding SEM micrographs for set A (Sirris, average HAZ size: 5 µm) and set B (Anyshape, average HAZ size: 1.3 µm).

The difference observed between the duration of the peaks of temperature for the two different sets of processing parameters can first be explained in terms of the input energy. This energy is equal to A921 $J.m^{-1}$ for set A (Sirris) while it is A284 $J.m^{-1}$ for set B (Anyshape) (here, the A coefficient stands for the laser absorptivity). The excess energy injected under the processing parameters of set A takes longer to be evacuated from the part, giving way to a large temperature peak. Moreover, the build platform temperature also plays a role: a higher build platform temperature (set A) leads to smaller thermal gradient and consequently to a decrease in heat conduction, which again tends to increase the width of the peak. These observations are in agreement with the experimental HAZ size shown in Fig. 7(b). The results from the FE simulations are thus consistent with the experimental observations.

Summary

A 2D FE model for the thermal history of LPBF of AlSi10Mg is developed and calibrated using experimental measurements of the melt pool height. In order to allow for the efficient simulation of the deposition of five successive layers, without incurring excessive computational cost, a remeshing procedure is implemented by keeping a constant number of nodes independently of the number of fused layers. The results from the multilayer FE simulations highlight that no heat accumulation is observed in LPBF AlSi10Mg under processing conditions corresponding to relatively low heat input. In this case, the thermal history of the HAZ is independent of the number of fused layers, and it can be studied using a thermal FE model for one single layer. Indeed, the influence of two different sets of processing parameters on the thickness of the HAZ is correctly predicted by single layer FE simulations.

Acknowledgements

The authors wish to acknowledge the financial support of the European Fund for Regional Development and the Walloon Region under convention FEDER “Iawatha” and of the Walinnov Longlife AM project, convention n°1810016, funded by the Service Public de Wallonie - Economie Emploi Recherche (SPW-EER). As Research Director of FRS-FNRS, A.M. Habraken acknowledges the support of this institution. The authors are also grateful to the CAREM of the University of Liège, for providing access to SEM facilities, and to Mr O. Rigo (Sirris) and Dr S. Michotte (AnyShape), for their help with samples fabrication.

References

[1] L. Thijs, K. Kempen, J.P. Kruth, J. van Humbeeck, Fine-structured aluminium products with controllable texture by selective laser melting of pre-alloyed AlSi10Mg, Acta Mater. 61 (2013) 1809-1819. https://doi.org/10.1016/j.actamat.2012.11.052

[2] E.O. Olakanmi, R.F. Cochrane, K.W. Dalgarno, A review on selective laser sintering/melting (SLS/SLM) of aluminium alloy powders: Processing, microstructure, and properties, Prog. Mater. Sci. 74 (2015) 401-477. https://doi.org/10.1016/j.pmatsci.2015.03.002

[3] A. Mertens, J. Delahaye, J. Lecomte-Beckers, Fusion-based additive manufacturing for processing aluminium alloys: state-of-the-art and challenges, Adv. Eng. Mater. 19 (2017) 1700003. https://doi.org/10.1002/adem.201700003

[4] ASM International (Hrsg.): ASM Handbook Volume 2: Properties and Selection: Nonferrous Alloys and Special-Purpose Materials, ASM International, 2004

[5] L. Roger, Fundamentals of aluminium metallurgy Production, processing and applications, Woodhead Publishing in materials: CRC Press, 2011.

[6] J. Delahaye, J.T. Tchuindjang, J. Lecomte-Beckers, O. Rigo, A.M. Habraken, A. Mertens, Influence of Si precipitates on fracture mechanisms of AlSi10Mg parts processed by Selective Laser Melting, Acta Mater. 175 (2019) 160-170. https://doi.org/10.1016/j.actamat.2019.06.013

[7] L. Zhao, J.G. Santos Macias, L. Ding, H. Idrissi, A. Simar, Damage mechanisms in selective laser melting AlSi10Mg under as-built and different post-treatment conditions, Mater. Sci. Eng. A 764 (2019) 138210. https://doi.org/10.1016/j.msea.2019.138210

[8] J. Delahaye, How to feed and validate a phase-field model predicting the evaluation of microstructures and properties in AlSi10Mg processed by Laser Powder Bed Fusion, PhD Thesis, University of Liège (Belgium), 2022. https://hdl.handle.net/2268/293324

[9] L. Zhao, L. Song, J.G. Santos Macías, Y. Zhu, M. Huang, A. Simar, Z. Li, Review on the correlation between microstructure and mechanical performance for laser powder bed fusion AlSi10Mg, Addit. Manuf. 56 (2022) 102914. https://doi.org/10.1016/j.addma.2022.102914

[10] A. Mertens, J. Delahaye, O. Dedry, B. Vertruyen, J.T. Tchuindjang, A.M. Habraken, Microstructure and properties of SLM AlSi10Mg: Understanding the influence of the local thermal history, Procedia Manuf. 47 (2020) 1089-1095. https://doi.org/10.1016/j.promfg.2020.04.121

[11] K.C. Mills, Recommended values of thermophysical properties for selected commercial alloys, Woodhead, Cambridge, 2002

[12] S. Cescotto, R. Charlier: Frictional contact finite elements based on mixed variational principles. Int. J. Numer. Methods Eng, 36 (1993) 1681-1701. https://doi.org/10.1002/nme.1620361005

[13] R. T. Jardin, V. Tuninetti, J. T. Tchuindjang, N. Hashemi, R. Carrus, A. Mertens, A. M. Habraken, Sensitivity analysis inthemodeling of a high-speed, steel, thin wall produced by directed energy deposition. Metals 10(11) (2020) 1554. https://doi.org/10.3390/met10111554

[14] S. Fetni, T. Maurizi Enrici, T. Niccolini, H. S. Tran, O. Dedry, L. Duchêne, A. Mertens, A. M. Habraken, Thermal model for the directed energy deposition of composite coatings of 316L stainless steel enriched with tungsten carbides, Materials & Design 204 (2021) 109661, https://doi.org/10.1016/j.matdes.2021.109661

[15] MSM & GEG (ULiege), 2022. Lagamine software [WWW Document]. Univ. Liege. URL http://www.lagamine.uliege.be/dokuwiki/doku.php (Accessed 4.12.22).

[16] M. Tang, P.C. Pistorius, S. Narra, J.L. Beuth, Rapid solidification: selective laser melting of AlSi10Mg, JOM 67 (2016) 960-966. https://doi.org/10.1007/s11837-015-1763-3

[17] I. Roberts, C.J. Wang, R. Esterlein, M. Stanford, D.J. Mynors, A three-dimensional finite element analysis of the temperature field during laser melting of metal powders in additive layer manufacturing, Int. J. Mach. Tools Manuf. 49 (2009) 916-923. https://doi.org/10.1016/j.ijmachtools.2009.07.004

[18] Y. Liu, J. Zhang, Z. Pang, Numerical and experimental investigation into the subsequent thermal cycling during selective laser melting of multi-layer 316L stainless steel, Opt. Laser Technol. 98 (2018) 23-32. https://doi.org/10.1016/j.optlastec.2017.07.034